



HAL
open science

Versatile and automated workflow for the analysis of oligodendroglial calcium signals

Dorien Maas, Blandine Manot-Saillet, Philippe Bun, Chloé Habermacher, Corinne Poilbout, Filippo Rusconi, Maria Cecilia Angulo

► **To cite this version:**

Dorien Maas, Blandine Manot-Saillet, Philippe Bun, Chloé Habermacher, Corinne Poilbout, et al.. Versatile and automated workflow for the analysis of oligodendroglial calcium signals. Cellular and Molecular Life Sciences, 2024, 81 (1), pp.15. 10.1007/s00018-023-05065-3 . hal-04583442

HAL Id: hal-04583442

<https://hal.inrae.fr/hal-04583442v1>

Submitted on 12 Jun 2024

HAL is a multi-disciplinary open access archive for the deposit and dissemination of scientific research documents, whether they are published or not. The documents may come from teaching and research institutions in France or abroad, or from public or private research centers.

L'archive ouverte pluridisciplinaire **HAL**, est destinée au dépôt et à la diffusion de documents scientifiques de niveau recherche, publiés ou non, émanant des établissements d'enseignement et de recherche français ou étrangers, des laboratoires publics ou privés.



HAL
open science

Versatile and automated workflow for the analysis of oligodendroglial calcium signals

Dorien A Maas, Blandine Manot-Saillet, Philippe Bun, Chloé Habermacher, Corinne Poilbout, Filippo Rusconi, Maria Cecilia Angulo

► **To cite this version:**

Dorien A Maas, Blandine Manot-Saillet, Philippe Bun, Chloé Habermacher, Corinne Poilbout, et al.. Versatile and automated workflow for the analysis of oligodendroglial calcium signals. Cellular and Molecular Life Sciences, 2024, 81 (1), pp.15. 10.1007/s00018-023-05065-3 . inserm-04399773

HAL Id: inserm-04399773

<https://inserm.hal.science/inserm-04399773>

Submitted on 17 Jan 2024

HAL is a multi-disciplinary open access archive for the deposit and dissemination of scientific research documents, whether they are published or not. The documents may come from teaching and research institutions in France or abroad, or from public or private research centers.

L'archive ouverte pluridisciplinaire **HAL**, est destinée au dépôt et à la diffusion de documents scientifiques de niveau recherche, publiés ou non, émanant des établissements d'enseignement et de recherche français ou étrangers, des laboratoires publics ou privés.

1 **Versatile and automated workflow for the analysis of oligodendroglial calcium signals**

2

3 Dorien A. Maas^{1*}, Blandine Manot-Saillet^{1*}, Philippe Bun², Chloé Habermacher^{1,6}, Corinne Poilbout¹,
4 Filippo Rusconi^{4,5}, Maria Cecilia Angulo^{1,3}

5

6 *1 Université Paris Cité, Institute of Psychiatry and Neuroscience of Paris (IPNP), INSERM U1266, "Team: Interactions*
7 *between neurons and oligodendroglia in myelination and myelin repair", F-75014 Paris, France*

8 *2 Université Paris Cité, Institute of Psychiatry and Neuroscience of Paris (IPNP), INSERM U1266, "Neurlmag*
9 *platform", F-75014 Paris, France*

10 *3 GHU PARIS psychiatrie & neurosciences, F-75014 Paris, France*

11 *4 IDEEV, GQE, Université Paris-Saclay, CNRS, INRAE, AgroParisTech, 12, route 128, F-91272 Gif-sur-Yvette, France*

12 *5 INSERM, UMR-S 1138, Centre de Recherche des Cordeliers, France; Sorbonne Université-INSERM, France*

13 *6 Present address: SynapCell, Bâtiment Synergy Zac Isiparc, F-38330 Saint Ismier, France*

14 * These authors contributed equally to this work

15

16 **Corresponding author:**

17 María Cecilia Angulo, Institute of Psychiatry and Neuroscience of Paris (IPNP), INSERM 1266, 102, rue de
18 la Santé, 75014 Paris, FRANCE. Tel: 33-1-40789243. e-mail address: maria-cecilia.angulo@u-paris.fr

19 **Abstract**

20 Although intracellular Ca^{2+} signals of oligodendroglia, the myelin-forming cells of the central nervous
21 system, regulate vital cellular processes including myelination, few studies on oligodendroglia Ca^{2+} signal
22 dynamics have been carried out and existing software solutions are not adapted to the analysis of the
23 complex Ca^{2+} signal characteristics of these cells. Here, we provide a comprehensive solution to analyze
24 oligodendroglia Ca^{2+} imaging data at the population and single-cell levels. We describe a new analytical
25 pipeline containing two free, open source and cross-platform software programs, Occam and post-
26 prOccam, that enable the fully automated analysis of one- and two-photon Ca^{2+} imaging datasets from
27 oligodendroglia obtained by either *ex vivo* or *in vivo* Ca^{2+} imaging techniques. Easily configurable, our
28 software solution is optimized to obtain unbiased results from large datasets acquired with different
29 imaging techniques. Compared to other recent software, our solution proved to be fast, low memory-
30 demanding and faithful in the analysis of oligodendroglial Ca^{2+} signals in all tested imaging conditions. Our
31 versatile and accessible Ca^{2+} imaging data analysis tool will facilitate the elucidation of Ca^{2+} -mediated
32 mechanisms in oligodendroglia. Its configurability should also ensure its suitability with new use cases
33 such as other glial cell types or even cells outside the CNS.

34

35 Keywords: oligodendrocytes, calcium imaging, microendoscopy, two-photon microscopy, open-source,
36 microscopy data analysis

37 Introduction

38 It is now established that Ca^{2+} signals of oligodendroglia, the myelinating cells of the central
39 nervous system, convert environmental information to cellular processes such as proliferation,
40 differentiation and myelination (Paez & Lyons, 2020; Pitman & Young, 2016; Maas et al., 2021). Primary
41 *in vivo* studies in the zebrafish revealed that both oligodendrocyte precursor cells (OPCs) and
42 oligodendrocytes (OLs) are capable of Ca^{2+} signaling (Baraban et al., 2018; Krasnow et al., 2018; Marisca
43 et al., 2020). In mouse brain slices, spontaneous Ca^{2+} activity in OPCs (Balía et al., 2017) and OLs (Battefeld
44 et al., 2019) is high during postnatal development when the myelination process is still ongoing, and
45 decreases in OLs as the brain matures (Battefeld et al., 2019). Then, Ca^{2+} signals of OLs are reactivated
46 upon demyelination in the adult mouse brain, suggesting that they play a crucial role in demyelinated
47 lesions (Battefeld et al., 2019). To date, compared to the large number of reports in other CNS cell types,
48 only few studies have explored *ex vivo* and *in vivo* oligodendroglia Ca^{2+} signaling under healthy and
49 pathological conditions. Moreover, in the above-mentioned studies, not only were the regions of interest
50 (ROIs) manually chosen, potentially introducing bias in the ROI selection outcome, but also complex Ca^{2+}
51 events with multiple peaks were overlooked even though these events are a hallmark of both OPCs and
52 OLs (see below).

53 Several software pipelines for the analysis of Ca^{2+} imaging data from both neurons and astrocytes,
54 in brain slices and *in vivo*, have been published. Unfortunately, problems arise when using neuron-
55 oriented programs such as CalmAn and EZCalcium for the analysis of oligodendroglial Ca^{2+} imaging data
56 (Cantu et al., 2020; Giovannucci et al., 2019). For instance, classifiers are used to recognize neurons as
57 round somata of a certain size (Giovannucci et al., 2019), while oligodendroglia possess less well-defined
58 shapes and sizes (Xu et al., 2021). Another important drawback of the available pipelines for neuronal Ca^{2+}
59 imaging is the difference in neuronal and oligodendroglial Ca^{2+} signal dynamics. Indeed, neuronal Ca^{2+}
60 signals last around 100 ms, are characterized by fast kinetics and occur with a high frequency (Chua &

61 Morrison, 2016). This is in stark contrast with OLs that exhibit complex Ca^{2+} dynamics, with signals that
62 last anywhere from several seconds to multiple minutes and that are characterized by slow rise and decay
63 times (our data and Battefeld et al., 2019). Another set of problems may arise when using available Ca^{2+}
64 imaging analysis for astrocytes in OL lineage cells: astrocytes are known to exhibit extensive signal
65 propagation within and between cells and Ca^{2+} signaling software pipelines such as AQUA are therefore
66 designed to trace Ca^{2+} events in time and space instead of identifying ROIs (Wang et al., 2019). Because
67 we cannot assume that intra- and inter-cellular signal propagation occurs extensively in OPCs and OLs,
68 these software pipelines are not readily suitable for the analysis of oligodendroglial Ca^{2+} signaling. Other
69 ROI-based astrocyte Ca^{2+} imaging analysis packages, such as GECIquant and CaSCaDe, are semi-
70 automated, which may introduce bias making them less desirable (Agarwal et al., 2017; Venugopal et al.,
71 2019) or, such as Begonia, are optimized for two-photon microscopy limiting the use to this imaging
72 modality (Bjornstad et al., 2021).

73 Here, we provide a comprehensive analytical pipeline-based package to explore oligodendroglial
74 Ca^{2+} imaging data obtained either *ex vivo* or *in vivo*. We developed two Free Open Source cross-platform
75 software programs, Occam and post-prOccam (Occam: Oligodendroglial cells calcium activity monitoring;
76 post-prOccam: post-processing of the data first output by Occam), for the fully automated analysis of one-
77 and two-photon Ca^{2+} imaging data from OPCs and OLs (GNU GPLv3+ license; code repository at:
78 <https://gitlab.com/d5674/occam>). These highly versatile and accessible tools are suitable for the analysis
79 of Ca^{2+} imaging datasets obtained with different imaging techniques and in diverse preparations, matching
80 the specific requirements for the monitoring of the complex Ca^{2+} event characteristics observed in OL
81 lineage cells. Our software should accelerate the elucidation of Ca^{2+} -mediated mechanisms in
82 oligodendroglia and might contribute to the development of therapeutic strategies in myelin-related
83 disorders such as multiple sclerosis.

84 **Materials and Methods**

85 **Experimental animals**

86 All the experiments followed European Union and institutional guidelines for the care and use of
87 laboratory animals and were approved by both the French ethical committee for animal care of the
88 University Paris Cité (Paris, France) and the Ministry of National Education and Research (Authorization
89 N° 13093-2017081713462292). They were performed with male and female *Pdgfra*^{CreERT(+/-)};*Gcamp6f*^{Lox/Lox}
90 or *Pdgfra*^{CreERT(+/-)};*Gcamp5-tdTomato*^{Lox/Lox} transgenic adult mice (7 to 9 weeks old) obtained by crossing
91 *Pdgfra*^{CreERT} (stock 018280, The Jackson Laboratory) with *Ai95(Rcl-Gcamp6f)-D* (stock 028865, The Jackson
92 Laboratory, USA) or *Gcamp5-tdTomato*^{Lox/Lox} (stock 028865, The Jackson Laboratory, USA). Animals were
93 genotyped by PCR using specific primers for Cre. All animals had *ad libitum* access to food and water and
94 were exposed to a 12 hr light/dark cycle, a controlled average temperature of 21 °C and 45% humidity
95 (see Supplementary Materials and Methods for details on experimental procedures on slice preparation
96 and demyelinated lesions).

97

98 **Ex vivo wide-field calcium imaging**

99 Cells expressing GCaMP6f in acute slices containing LPC-induced demyelinated lesions of corpus callosum
100 were visualized with a 40x water immersion objective in a wide-field microscope (NA: 0.80, Olympus BX51)
101 using a LED system (CoolLED PE-2; Scientifica, UK) and a CCD camera (ImageQ, Optimos; Scientifica, UK)
102 (Supplementary Materials and Methods; Mozafari et al., 2020). Excitation and emission wavelengths were
103 obtained by using 470 nm and 525 nm filters, respectively (Ref: 49002; Chroma, USA). The CCD camera
104 and the LED system were controlled using a Digidata 1440A interface and Pclamp10.5 software (Molecular
105 Devices, USA). The image stacks were acquired at a frame rate of 1.75 Hz with 50 ms light exposure for a
106 total duration of 240 s using Micro-manager-1.4 plugin under the Fiji/ImageJ2 framework (version 1.53k
107 or later) (Schindelin et al., 2012). In few cases, we observed GcaMP6f⁺ vascular cells in demyelinated

108 lesions at 7 days post-LPC injections (dpi), *i.e.* two weeks after the first tamoxifen injection (50 mg/kg per
109 injection; Supplementary Fig. 1d), that may correspond to PDGFR α -expressing perivascular fibroblasts.
110 Easily identified by their vascular shape, we could discard the fields containing these cells during the
111 experiment or the analysis. Ca²⁺ imaging during bath applications of 50 μ M carbachol were performed
112 after incubating the slices for five minutes with an antagonist cocktail containing 10 μ M NBQX, 50 μ M
113 AP5, 10 μ M GABA_Azine, 1 μ M TTX and 50 μ M mecamylamine.

114

115 ***Ex vivo* two-photon calcium imaging**

116 Two-Photon Ca²⁺ imaging of putative GCaMP5⁺ OPCs and OLs in acute slices of LPC-induced demyelinated
117 lesions of corpus callosum was performed using a two-photon laser scanning microscope and acquired in
118 frame mode (150-250 ms per frame) with custom-made software (LabVIEW, National Instruments) as
119 previously described (Otsu et al., 2014; Balia et al., 2017). Briefly, a 40x water-immersion objective
120 (Olympus40x LumPlanFL N 540x/0.8) in combination with a 900 nm excitation beam from a femtosecond
121 Ti:Sapphire laser (10 W pump; Mira 900 Coherent, Santa Clara, CA) was used to image GcaMP5 in areas
122 sized 1148-2000 μ m². GcaMP5 was detected with Hamamatsu photon counting PMTs through an
123 emission filter (HQ500/40, Chroma). Pixel dwell time was fixed at 6.2 μ s. Ca²⁺ signals of individual cells
124 were imaged at 3.60-6.27 frames per second during 99 seconds. To distinguish OPCs and OLs, we used
125 morphological criteria and recorded only cells for which we could connect the processes to a particular
126 soma. In corpus callosum, OPCs were characterized by a relatively small round soma and a stellate
127 arborization with thin processes whereas OLs had a larger soma and principal processes often aligned with
128 axons.

129

130 **Occam and post-prOccam: Ca²⁺ signal analysis software programs for the investigation of**
131 **oligodendroglia**

132 The imaging data analysis is performed in two steps by the two distinct software pieces thoroughly
133 described in the Results section and in the software user manual provided as supplementary information
134 (Supplementary manual). Briefly, the Occam program first processes the image stack producing data
135 stored in a set of files that are then processed by the post-prOccam program for data refinement and
136 statistical calculations. Occam is a Fiji/ImageJ2-based plugin written in Java (Fiji/Imagej2 framework
137 version 1.53k or later) and post-prOccam is written in Python3. One important feature of our software
138 package is that both Occam and post-prOccam can be extensively configured to adapt the processing to
139 *ex vivo* wide-field, *ex vivo* two-photon or *in vivo* microendoscopic Ca²⁺ imaging stacks. The configuration
140 allows for an optimized processing of the Ca²⁺ signals acquired in these different preparations (see
141 configuration file examples for each condition in Supplementary Files 1-3; Supplementary manual). The
142 software described in this report is cross-platform Free and Open Source Software (FOSS) and licensed
143 under the GNU GPLv3+ license (code and documentation are available at:
144 <https://gitlab.com/d5674/occam>).

145

146 **Benchmarking two other software offerings against Occam/post-prOccam**

147 Our software package was benchmarked against other available software. To this end all of our datasets
148 used in this study were reanalyzed with GECIquant and AQuA, two programs running under the same
149 Fiji/Imagej2 framework (Venugopal et al., 2019; Wang et al., 2019). To minimize the comparison bias, all
150 the user-settable parameters were optimally tuned for each tested program in each imaging condition.
151 All the comparisons of the three software programs were performed with the same parameters of spatial
152 and temporal resolution (pixel size, acquisition rate) and minimal pixel size (300 pixels for *ex vivo* wide-
153 field, 20 pixels for *ex vivo* two-photon microscopy, 80 pixels for *in vivo* microendoscopy). The benchmark
154 was run on a computer under the Debian GNU/Linux version 11 operating system (DELL Latitude, Intel(R)
155 Xeon(R), CPU E3-1505M v6 @ 3.00GHz, 4 cores, Graphics NVIDIA Quadro M1200, 32 Gb RAM). For AQuA,

156 additional parameters were set as follows: Intensity threshold scaling factor: 5, for *ex vivo* wide-field; 2-3,
157 for *ex vivo* two-photon microscopy and 2-3, for *in vivo* microendoscopy; Smoothing: 1; Temporal cut
158 threshold: 3; Growing z threshold: 1; Rising time uncertainty: 2; Slowest delay in propagation: 1;
159 Propagation smoothness: 1; Z score threshold: 2.

160

161 **Automated analysis of Ca²⁺ signals from OPCs, OLs and myelin sheaths in different species and imaging** 162 **conditions**

163 Our software package was tested on datasets from OPCs, OLs and myelin sheaths acquired using one-
164 photon or two-photon microscopy in different laboratories. Since these images were acquired at different
165 magnifications and in different microscopy set-ups, we trained WEKA plugin separately with each image
166 stack to generate specific classifiers. Then, we proceeded to the automated analysis with Occam by setting
167 a minimal pixel size at 20, except for OPCs in zebrafish for which we used a minimal pixel size of 10. Occam
168 was configured as *ex vivo* two-photon microscopy for cells recorded in mouse preparations and zebrafish
169 myelin processes in zebrafish and *in vivo* wide-field for OPCs in zebrafish. The other parameters were set
170 as default values in mouse preparations. For zebrafish, we used a spatial binning value of 2 for myelin
171 sheaths and the following parameters for OPCs: overlap: 30%, binning value 1, temporal trimming value
172 12, spatial trimming value 40, number of frames in the substack: 2. For each analyzed image stack, the
173 parameters in the configuration file used by post-prOccam were set according to the acquisition rate and
174 the area of the images and adjusted according to the recording conditions and noise. ROI trace correction
175 was always performed using $\Delta F/F$.

176

177 **Statistical analysis**

178 Data are expressed as mean \pm SEM. GraphPad Prism (version 9.3.0; GraphPad Software Inc., USA) was
179 used for statistical analysis. Each group of data was first subjected to Shapiro-Wilk normality test.

180 According to the data structure, two-group comparisons were performed using the two-tailed unpaired
181 Student's t-test or the non-parametric two-tailed unpaired Mann-Whitney U test for independent
182 samples; the two-tailed paired Student's t-test was used for paired samples. Multiple comparisons were
183 done with a one-way ANOVA test followed by a Tukey's multiple comparison test, the non-parametric
184 Friedman test followed by a Dunn's multiple comparison test or the two-way ANOVA test followed by a
185 Bonferroni's multiple comparison test.

186

187 Results

188

189 Occam performs automated noise correction and ROI definition

190 The goal of this study was to develop a fully automated analytical workflow for the investigation
191 of one- and two-photon intracellular Ca²⁺ imaging data from OPCs and OLs in *ex vivo* and *in vivo*
192 preparations. We developed the Occam and post-prOccam software programs for this purpose by initially
193 using wide-field Ca²⁺ imaging stacks in acute slices obtained in mouse corpus callosum demyelinated
194 lesions. Because in this kind of imaging condition OPCs and OLs expressing cytosolic GCaMP6f are
195 indistinguishable (Sahel et al., 2015), we hereinafter refer to these cells with the generic term
196 oligodendroglia. We later expanded the scope of the software by implementing new features for the
197 analysis of two-photon Ca²⁺ imaging stacks of single OPCs and OLs and *in vivo* microendoscopy Ca²⁺ imaging
198 stacks of oligodendroglia using a miniscope (Fig. 1). Our software was initially developed and validated for
199 the processing of imaging data obtained in demyelinated lesions in mouse models where the GCaMP
200 protein is not expressed in OL lineage cells in healthy white matter (*Pdgfra*<sup>CreERT(+/-);Gcamp6f^{Lox/Lox} or
201 *Pdgfra*<sup>CreERT(+/-);Gcamp5-tdTomato^{Lox/Lox}; Supplementary Fig. 1). We further validated its use on Ca²⁺
202 imaging datasets from OPCs, OLs and myelin sheaths in control conditions and in different species and
203 imaging setups from different laboratories working on Ca²⁺ signals of these cells (see below).</sup></sup>

204 *Bleaching and noise correction.* The data input to Occam is a Ca²⁺ imaging stack of frames recorded
205 by microscopy acquisition software (see Supplementary Videos 1-3 as different examples). Occam
206 performs specific processing steps for image stacks originating from different Ca²⁺ imaging conditions.
207 These processing steps are summarized in Figure 1a and in Supplementary manual. In the case of *ex vivo*
208 wide-field Ca²⁺ imaging stacks, Occam first performs a bleaching correction step because this imaging
209 condition often produces significant photobleaching (Fig. 1a; Supplementary Video 1). Such correction is

210 not needed for imaging stacks originating in two-photon or microendoscopy experiments (Fig. 1a;
211 Supplementary Video 2-3).

212 To correct for photobleaching, Occam fits the mean fluorescence intensity over time with a
213 double exponential decay curve as follows:

$$214 \quad y = A + B \cdot \exp(-C \cdot t) + D \cdot \exp(-E \cdot t)$$

215 where A is the offset of the intensity, B and D are the amplitude of each exponential and C and E are the
216 characteristic time decay values of the t exponential. In this procedure, we encountered a difficulty in
217 fitting the fluorescence decay due to large fluctuations in the mean intensity resulting from the high
218 spontaneous Ca²⁺ activity in oligodendroglia. To overcome this problem, we adapted the fitting procedure
219 by generating several possible fits of the trace after removing sections with variable size and position. At
220 the end of this step, a series of graphs are displayed showing the mean fluorescence intensity over time,
221 the fit, the corrected mean fluorescence intensity of the image stack to which the fit applies, and the
222 goodness of the fit (Supplementary manual). The user can then select the best fit for bleaching-correction
223 step. If no single fit gives a reliable correction, the user can decide to skip this bleaching-correction step.
224 Finally, the ratio between the raw and the fitted mean fluorescence intensity is calculated to obtain the
225 corrected mean fluorescence intensity over time.

226 The software then performs noise corrections. For this step, we empirically tested different filter
227 combinations allowing to both reduce the noise and increase the contrast. Wide-field image stacks from
228 acute brain slices were the noisiest and required a combination of a Fourier transform filter, a rolling ball
229 background subtraction and a Gaussian blur. Since the signal-to-noise ratio is better in image stacks from
230 two-photon and miniscope images, their quality was not highly improved by this procedure, but we kept
231 this correction to process all of the images for the next steps of segmentation in a similar fashion. In the
232 miniscope experimental setting, the software configuration did not involve any use of the Fourier
233 transform filter, which accelerates the data processing.

234 The noise-corrected image stack is then used to generate one image (called projection image) that
235 will be used for the segmentation step (Fig. 1a). To define the most suitable projection image to perform
236 the segmentation, we first tested several simple projection images, such as the standard deviation
237 intensity projection. We found that simple projections were insufficient to detect all fluorescence
238 fluctuations, which prompted us to test the combination of several types of projections into one single
239 final projection image to improve the contrast. Through trial and error, we found that the best projection
240 image in the case of wide-field and two-photon imaging stacks was obtained by summing the maximum
241 intensity projection and the sum intensity projection. For miniscope image stacks, instead, the best
242 projection image was produced by multiplying the maximum intensity projection with the standard
243 deviation projection (Fig. 1a). The data processing performed by Occam to generate the final projection
244 image thus depends on the Ca^{2+} imaging configuration mode set by the user upon starting of the
245 processing (wide-field, two-photon and miniscope).

246 *Designation of active ROIs.* Occam performs the automatic ROI designation by harnessing the
247 machine learning-based WEKA Fiji/ImageJ2 plugin that performs a trainable segmentation of frames
248 (Arganda-Carreras et al., 2017) combined with a local maxima segmentation tool (Fig. 1a; Fig. 2a). First,
249 WEKA is manually trained with the Occam-generated projection image to produce ROI classifiers for the
250 three distinct imaging conditions, namely wide-field, two-photon, and miniscope. This training only takes
251 a few minutes and is performed once with 3-5 projection images obtained from a subset of the image
252 stacks originating in a given experiment setting. A minimum of two training classes are required to train
253 WEKA and to produce a pixel-based segmentation (see below). We found, however, that four classes do
254 better maximize the detection of regions with fluorescence intensity fluctuations (see Arganda-Carreras
255 et al., 2017 for details of WEKA plugin). We named these classes 1) high, 2) medium, 3) low and 4)
256 background matching their relative mean pixel intensities. High and medium classes define regions with
257 very high and intermediate pixel intensities, respectively, and therefore represent those that most likely

258 detect true fluorescence changes. These regions are considered as active ROIs during data analysis while
259 low and background mean pixel intensity ROIs (dark and very dark, respectively) are considered as
260 background and are discarded. During data processing, the ROI classifier and WEKA are called by Occam
261 to obtain a first segmentation. However, because WEKA needs training by the user, its operation while
262 performing the segmentation might suffer from some bias. To overcome this potential problem, Occam
263 combines the results obtained by WEKA with those obtained by an automatic and unsupervised
264 segmentation based on local maxima. Of note, this procedure was designed to detect ROIs showing
265 fluorescence fluctuations and not ROIs having constant fluorescence values because the projection image
266 used for the segmentation mainly reveals fluorescence changes. At the end of the segmentation
267 procedure, Occam designates a ROI as a vector of mean fluorescence intensity values of the corresponding
268 region in the different frames of the stack (that is, over the acquisition time points). Such ROI vectors are
269 also indifferently called ROI traces or ROIs in this report.

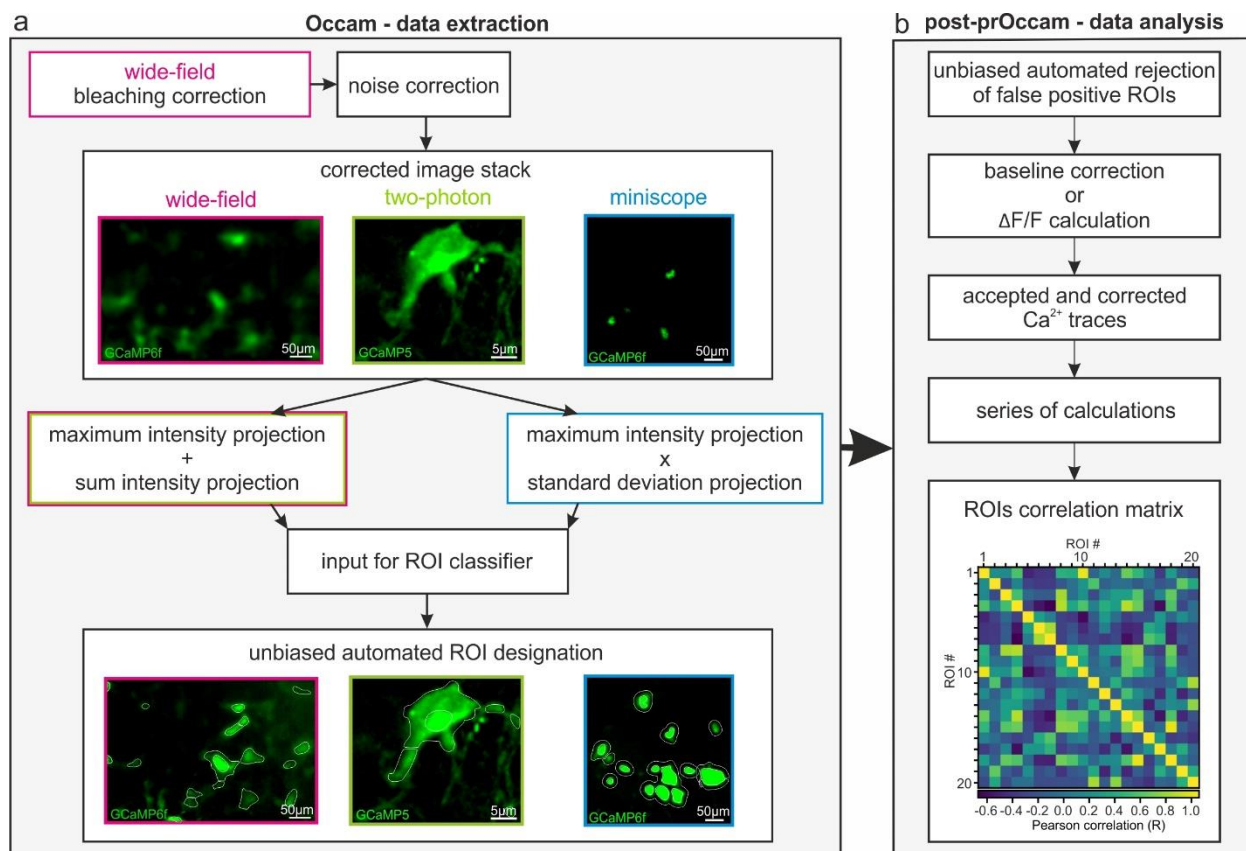
270 Datasets obtained by *in vivo* imaging proved particularly challenging because the large number of
271 frames in the stacks (as a result of long acquisition times) yielded a useless projection image, because Ca^{2+}
272 signals might have occurred either as a too short event or as a too intense and prolonging event. To
273 enhance the precision of ROI detection by Occam in such large data files, the program first splits the image
274 stack into a configurable number of sub-stacks that are in turn processed as described above to yield a
275 projection image for each sub stack (Fig. 3a). Another challenge that we encountered is that this
276 procedure can lead to an overestimation in the number of active ROIs if a specific region of the stack is
277 active several times during a single experiment and is thus detected as a different ROI in multiple sub-
278 stacks. In this specific situation, the user can configure a setting value defining the ROI overlapping
279 tolerance level above which overlapping ROIs are merged into a single ROI (Fig. 3a; Supplementary
280 manual). The described procedure segments large image stacks from either a single acquisition or from
281 multiple acquisitions performed on the same animal over weeks (Fig. 3a-f).

282 From a user experience stand point, Occam features a graphical user interface that allows the
283 user to easily and intuitively configure various aspects of the data processing. In particular, the user selects
284 one configuration predetermined for the analysis of oligodendroglia Ca^{2+} imaging stacks from one of the
285 three supported imaging conditions, namely i) wide-field, ii) two-photon and, iii) miniscope imaging
286 stacks, (Fig. 1a; Supplementary Video 1-3). The Occam program can therefore be used for automated and
287 customizable detection of active ROIs in Ca^{2+} imaging stacks and even allows for precise segmentation in
288 large stacks obtained during long recordings. Additionally, Occam makes the preprocessing of longitudinal
289 *in vivo* Ca^{2+} imaging experiments feasible with quick image segmentations for data obtained over multiple
290 days or weeks.

291 To further confirm that Occam successfully performs ROI designation, we tested the program on
292 two simulated datasets which allow us to independently examine two different situations: 1) transient
293 objects with different sizes and shapes, and 2) different objects changing location (freely available at
294 <https://github.com/yu-lab-vt/AquA; Wang et al., 2019>). The first situation was analyzed using the two-
295 photon configuration which allows for the visualization of isolated events, while the second one was
296 analyzed using the miniscope configuration which captures brief overlapping events. In the two different
297 conditions, Occam's ROIs fit the shape of almost all events (Supplementary Fig. 2). Using five consecutive
298 images of the stack to quantify the number of detected ROIs, we found that Occam detected 38 out of 37
299 objects in the first case (Supplementary Fig. 2a) and 26 out of 28 objects in the second case
300 (Supplementary Fig. 2b, c), confirming that it is capable of detecting most of the events in simple and
301 complex situations.

302 Upon processing of any given image stack of frames, Occam produces a corresponding set of
303 tabular data files that contain descriptions of the mean fluorescence intensity of each ROI along the time-
304 resolved acquisition experiment. These files are then fed to the post-prOccam software for ROI
305 refinement and statistical calculations (Fig. 1b).

306



307

308 **Figure 1 – Occam and post-prOccam: an automated analysis software solution for oligodendroglia Ca^{2+}**
309 **imaging of different preparations. (a)** The Occam software is available as a Fiji/ImageJ2 plugin and
310 configurable for the analysis of wide-field, two-photon and *in vivo* microendoscopy Ca^{2+} imaging. Occam
311 performs bleaching correction only on wide-field image stacks and does noise correction according to the
312 imaging condition (Supplementary manual). Then, it uses the maximum and sum intensity projections for
313 wide-field and two-photon image stacks and the maximum and standard deviation projections for
314 miniscope image stacks to build a projection image used as input for the WEKA-based ROI classifier. **(b)**
315 Output from Occam is fed to the post-prOccam Python-based software that 1) rejects any ROI that does
316 not show significant Ca^{2+} fluctuations; 2) performs either baseline subtraction or the conventional $\Delta F/F$
317 correction; 3) performs statistical calculations for each accepted ROI; and 4) computes a ROIs Pearson
318 correlation matrix. Occam and post-prOccam are multiplatform, free and open source programs, freely
319 available at: <https://gitlab.com/d5674/occam> (detailed procedures and software inner workings are
320 described in the Supplementary manual).

321

322

323

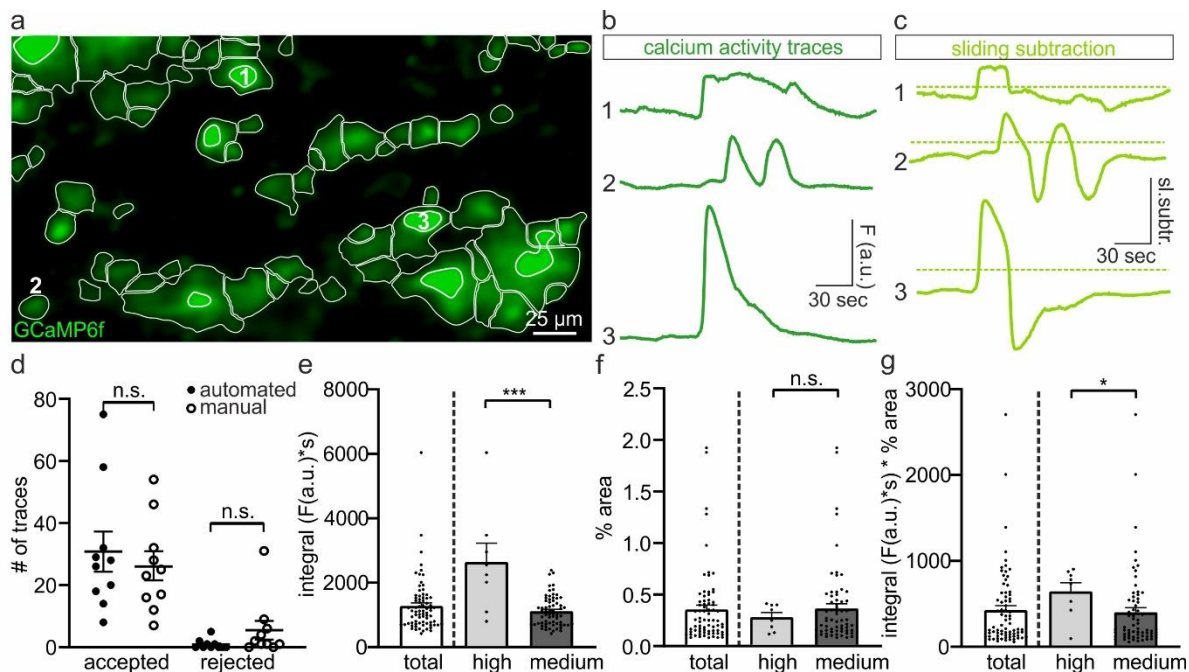
324

325 **post-prOccam performs automated ROI refinement, quantifications and correlations**

326 The post-prOccam software processes the files produced by Occam according to user-defined
327 settings determining the ROI processing and filtering stringency, as defined in a configuration file
328 (Supplementary Files 1-3).

329 *Rejection of false positive ROIs.* First, post-prOccam was designed to reject false positive ROIs (Fig.
330 1b). Automated ROI detection algorithms cannot be error-free and almost always require post-processing
331 aimed at rejecting false positive ROIs (Cantu et al., 2020). To reject false positive ROIs, we adapted an
332 algorithm previously used for the fluorescence-based tracking of exocytotic events (Yuan et al., 2015;
333 Supplementary manual). Based on repeated intensity value subtractions in a sliding window over the
334 whole ROI vector of mean fluorescence intensity values (Supplementary Fig. 3a-c), our method allowed
335 us to detect fluorescence intensity changes that were greater than noise fluctuations. For this, we had to
336 take into account the long-lasting kinetics of Ca²⁺ signals from OPCs and OLS in the three tested imaging
337 conditions (Supplementary Fig. 4). In the case of wide-field image stacks, for instance, the sliding window
338 subtractions were computed between points distanced by 40 frames, a value close to the measured rise
339 time of several Ca²⁺ events (Fig. 2b-c; Supplementary Fig. 4a; rise time: 54.63±9.67 frames equivalent to
340 35.25±5.36 s, n=34 events from n=8 fields). The sliding window subtraction is performed according to the
341 following calculation: $ROI'[n] = ROI[n+40] - (ROI[n])$, with n being the frame number in the stack (n is
342 incremented by 1 after each such calculation; Supplementary Fig. 3a-c). Each initial ROI trace is thus
343 replaced by a new one, as computed from the sliding window subtractions, that is then tested against
344 user-defined threshold parameters set in the configuration file (Supplementary Files 1). These threshold
345 settings configure the rejection of ROI traces depending on both their Ca²⁺ event kinetics and noise. To
346 find the best settings to eliminate false positive traces, we empirically tuned the threshold parameters
347 and compared the results with those obtained by manually rejecting ROIs in several imaging stacks (Fig.
348 2d). The threshold values that were found to be the most effective in rejecting false positive ROIs were a

349 sliding subtraction window of 40 points and a mean absolute deviation factor of 1.5 based on Ca^{2+} signal
 350 characteristics and the noise fluctuations, and were set as default values in the configuration file provided
 351 in Supplementary File 1 (Fig. 2a-c; see the detailed description of the threshold parameters in the
 352 Supplementary manual). A similar procedure was applied for determining the most suitable parameters
 353 to analyze two-photon and miniscope image stacks (Supplementary File 2-3).



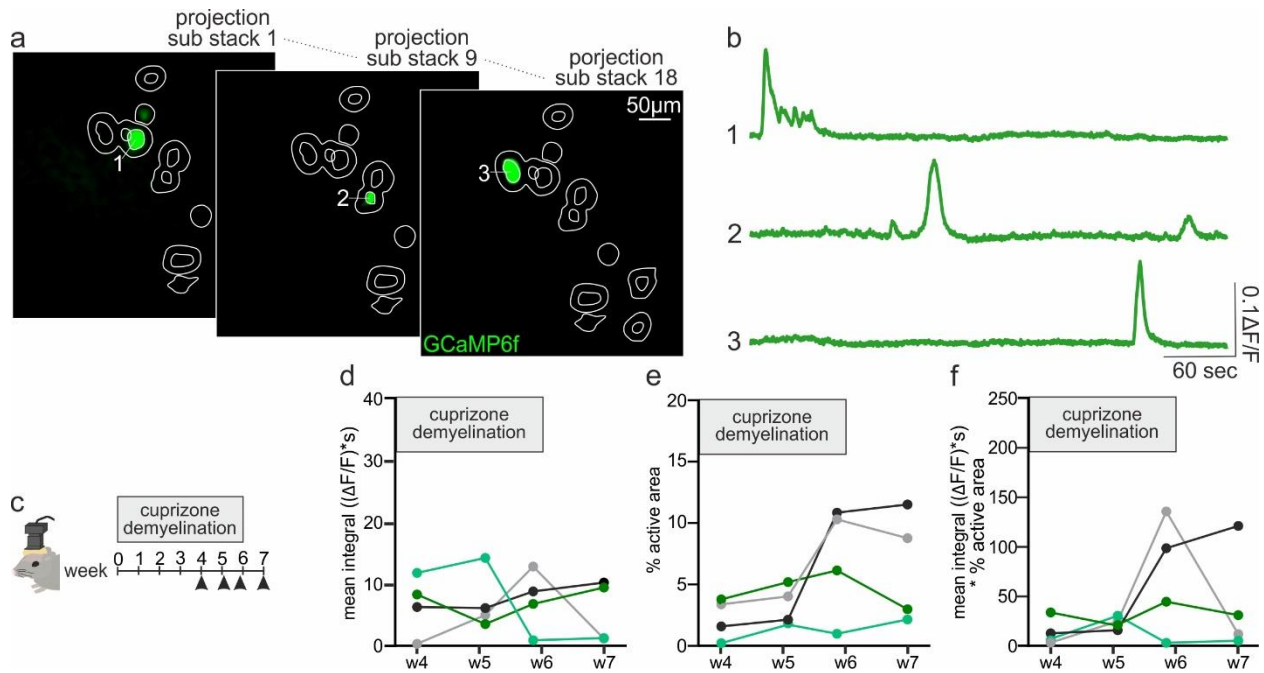
354
 355 **Figure 2 – Analysis of wide-field Ca^{2+} signals of oligodendroglia in brain slices.** (a) Representative
 356 projection image output by Occam with designated active ROIs (white) obtained from a 40x wide-field
 357 fluorescence imaging stack with GCaMP6f-expressing oligodendroglia in mouse callosal LPC-induced
 358 lesion. (b and c) Representative corrected ROI traces (b) and sliding window subtraction traces (c) as
 359 obtained with post-prOccam. (d) Comparison of the manual rejection of false positive ROIs and the
 360 automatic rejection of false positive ROIs by post-prOccam revealed no differences in accepted and
 361 rejected ROIs, validating post-prOccam’s performance. n.s.: not significant, two-way ANOVA followed by
 362 a Bonferroni multiple comparisons test. (e-g) Calculations performed by post-prOccam on each individual
 363 ROI of the image stack include the integral (e), the percentage of active area (f) and the integral multiplied
 364 by the percentage of active area (g). The calculations are performed separately for high and medium
 365 intensity ROIs. * $p < 0.05$ and *** $p < 0.001$; Mann-Whitney test.
 366

367 *ROI trace correction.* ROIs that are accepted by post-prOccam for further analysis are then
 368 corrected either by performing a baseline subtraction or by calculating $\Delta F/F$, as defined by the user in the
 369 configuration file (Fig. 1b; Supplementary manual and Files 1-3). In the case of baseline subtraction, the

370 mean minimum intensity value calculated from a configurable number of trace points around the
371 minimum intensity value of the ROI is subtracted from the ROI trace whereas, in the case of $\Delta F/F$ trace
372 correction, the $\Delta F/F = [(F(t)-F_0)/F_0]$ computation is performed on the ROI trace (F_0 is the mean minimum
373 intensity value). We implemented these two options because in the case of wide-field microscopy, we
374 found that a baseline subtraction computation was better adapted than the conventional $\Delta F/F$ to the
375 analysis of the oligodendroglia Ca^{2+} signal dynamics. Indeed, the oligodendroglial cells in acute brain slices
376 exhibited overall high levels of background noise and high levels of spontaneous Ca^{2+} activity, often right
377 at the start of the recording, making it difficult to determine with certainty the real F_0 resting fluorescence
378 intensity value (Fig. 2a-b, Supplementary Fig. 4a, d-e). For two-photon and miniscope imaging stacks,
379 determination of the resting fluorescence was feasible and therefore we used the $\Delta F/F$ ROI trace
380 correction option (Fig. 3b; Fig. 6a, e).

381 *Statistical calculations on corrected ROI traces.* The accepted and corrected ROI traces are output
382 to a file for further statistical processing, such as, for example, the calculation of the surface area of each
383 ROI in pixels, the ROI integral, the sum of all the ROIs integrals and of all the ROIs surface areas in pixels.
384 The results of these calculations are output to a file (Fig. 1b; Supplementary manual). Figure 2e-g illustrate
385 calculation results obtained on each ROI in a single image stack; Figure 3d-f show the calculation results
386 for all the ROIs in several image stacks from four mice recorded during several weeks. Since the complex
387 features of oligodendroglial Ca^{2+} events make it difficult their proper individual isolation (Supplementary
388 Fig. 4), we found it more appropriate to calculate the mean intensity integral of each ROI trace rather than
389 to use a procedure for single event detection (Balía et al., 2017; see Discussion). When using single event
390 detection procedures, complex events are oversimplified even though they are characteristic of both OPCs
391 and OLs and should therefore be taken into account (Fig. 6, Supplementary Fig. 4). Using the mean
392 intensity integral of the ROI trace implies that all Ca^{2+} events in their entirety are considered in the
393 analysis. As expected, high intensity ROIs exhibited significantly larger mean integrals than medium

394 intensity ROIs (Fig. 2e) and, despite similar mean percentage of active area between high and medium
 395 intensity ROIs (Fig. 2f), the mean integral multiplied by the percentage of the active area remained larger
 396 for high intensity ROIs (Fig. 2g). However, when considering all the analyzed stacks, the number of high
 397 intensity ROIs was always considerably smaller than the number of medium intensity ROIs (high intensity
 398 ROIs: $n=3.5\pm0.9$; medium intensity ROIs: $n=27.3\pm5.7$; total ROIs: $n=30.8\pm6.5$ for $n=10$ stacks, $N=7$ mice).
 399 Moreover, the mean integral of medium intensity ROIs and that of all pooled data (Total) remain similar
 400 (Fig. 2e). Therefore, the data from high and medium intensity ROIs are pooled by post-prOccam for
 401 subsequent quantifications; however, we kept their Occam-based detection separate because the WEKA
 402 plugin performed better when classifying ROIs in these two categories.

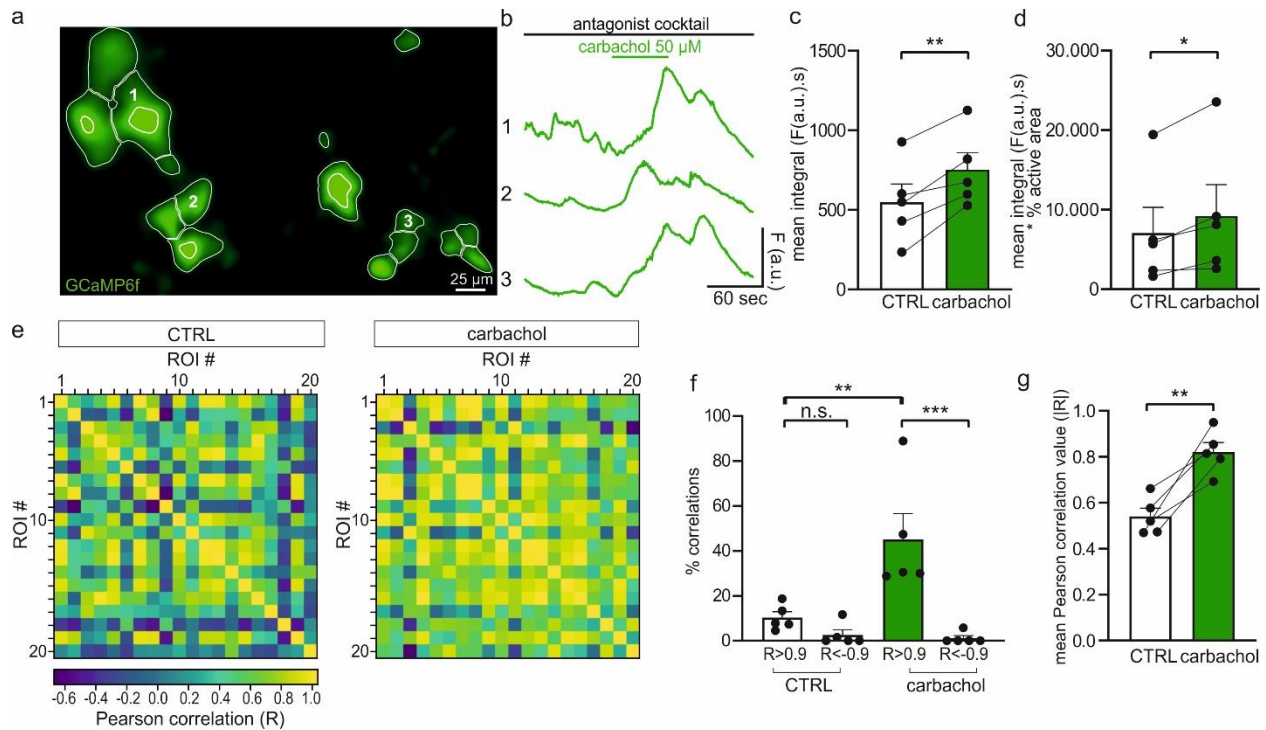


403

404 **Figure 3. Analysis of *in vivo* microendoscopy Ca²⁺ signals of oligodendroglia in freely moving mice.** (a)
 405 Representative images of an *in vivo* microendoscopy Ca²⁺ imaging stack collected from a demyelinated
 406 corpus callosum of a freely moving mouse. The image displays detected active ROIs (white) in several sub-
 407 stacks as obtained with the *in vivo* analysis option of Occam and (b) their corresponding corrected Ca²⁺
 408 traces obtained with post-prOccam. (c) Longitudinal experiments that can be analyzed with Occam and
 409 post-prOccam over weeks. Four mice were fed with the cuprizone diet to induce demyelination (see
 410 Supplementary Material and Methods) and Ca²⁺ imaging was performed for four consecutive weeks. (d)
 411 Mean integral, (e) % of active area and (f) mean integral multiplied by percentage of active area are
 412 calculated with post-prOccam over the four consecutive weeks for all mice.

413

414 *ROI interval-based analysis.* One important feature of post-prOccam is its ability to compare ROIs
415 only at specific acquisition time point intervals of the recorded datasets. For instance, in the case of
416 applications of pharmacological agents during Ca²⁺ imaging recordings, a user might wish to compare Ca²⁺
417 signals in the absence or in the presence of a drug in a single image stack. The default post-prOccam
418 software behavior is to perform all the calculations described in the previous sections on the whole ROI
419 vector (that is, for all the acquisition time points). However, in the specific cases mentioned above, it
420 might be useful for the calculations to be performed only over selected ranges of the ROI vector (that is,
421 intervals of that ROI's acquisition time points). The configuration file provides a section in which the user
422 might list any number of ROI vector intervals over which to perform the previously described calculations
423 (Supplementary Files 1-3). To validate this feature, we bath-applied the muscarinic receptor agonist
424 carbachol in the presence of a cocktail of antagonists to stimulate intracellular Ca²⁺ signals of
425 oligodendroglia during wide-field Ca²⁺ imaging recordings (Fig. 4a, b). Oligodendroglia express muscarinic
426 receptors M1, M3 and M4, which, when activated by carbachol, increase intracellular Ca²⁺ signals
427 (Abiraman et al., 2015; Cohen & Almazan, 1994; Welliver et al., 2018). Our tests showed that post-
428 prOccam can indeed detect the expected increase in intracellular Ca²⁺ signals in oligodendroglia upon bath
429 application of 50 μM carbachol in the presence of a cocktail of antagonists, as revealed by an increase in
430 the mean integral compared to control conditions (before carbachol application; Fig. 4a-d).



431

432 **Figure 4. ROI interval-based analysis and evaluation of Ca^{2+} signal synchronization in oligodendroglia.**
 433 **(a)** Representative image of Ca^{2+} imaging in callosal LPC-induced lesions in *ex vivo* brain slices that were
 434 exposed to 50 μM carbachol to induce increases in Ca^{2+} signals in oligodendroglia in the presence of an
 435 antagonist cocktail containing 10 μM NBQX, 50 μM AP5, 10 μM GABAazine, 1 μM TTX and 50 μM
 436 mecamylamine. The image displays detected active ROIs (white) as obtained with Occam. **(b)**
 437 Representative corrected Ca^{2+} traces obtained with post-prOccam from callosal LPC-induced
 438 demyelinated lesions in brain slices that were exposed to 50 μM carbachol to induce an increase in Ca^{2+}
 439 signals in oligodendroglia in the presence of a cocktail of antagonists containing 10 μM NBQX, 50 μM AP5,
 440 10 μM GABAazine, 1 μM TTX and 50 μM mecamylamine. **(c and d)** Mean integral (c) and mean integral
 441 multiplied by the percentage of active area (d) of Ca^{2+} signals in control and after exposure to carbachol.
 442 * $p < 0.05$, ** $p < 0.01$; paired Student's t-test. **(e)** Example of correlation matrices obtained with post-
 443 prOccam before and after carbachol exposure. Each square indicates the Pearson correlation value of one
 444 ROI with another. Yellow indicates high positive Pearson correlation, while dark blue indicates high
 445 negative correlations. Note that traces 1, 2, 3 in panel a correspond to ROIs 7, 12, 14 in the matrix. **(f)** The
 446 percentage of correlations in the correlation matrix that is significantly negative ($R < -0.9$) or significantly
 447 positive ($R > 0.9$) in both control and carbachol exposed conditions. n.s.: not significant, ** $p < 0.01$,
 448 *** $p < 0.001$, two-way ANOVA followed by a Tukey's multiple comparisons test. **(g)** Mean Pearson
 449 correlation values for control and carbachol conditions. CTRL: control before carbachol exposure ($n = 5$
 450 stacks, $n = 5$ slices, $n = 4$ mice). Note that post-prOccam successfully identified the expected enhanced
 451 synchronization of Ca^{2+} signals upon carbachol application, validating its correlation analysis capabilities.
 452 ** $p < 0.01$; paired Student's t-test. CTRL: control before carbachol exposure ($n = 5$ stacks, $n = 5$ slices, $n = 4$
 453 mice). Dot plots are presented as mean \pm s.e.m.
 454

455 *Analysis of synchronized Ca^{2+} signals.* While it is now established that a population of astrocytes
 456 may exhibit high levels of Ca^{2+} activity synchronization *in vitro* and *in vivo* (Ingiosi et al., 2020; Koizumi,

2010), nothing is known about the potential of Ca^{2+} signals in oligodendroglia to be synchronized. We thus implemented in post-prOccam a correlation calculation which allows the user to establish whether ROIs within a given image stack show synchronized Ca^{2+} signals. The post-prOccam program computes an inter-ROI Pearson correlation coefficient matrix between each ROI trace and every other ROI trace (Fig. 4e; see Materials and Methods; Ingiosi et al., 2020). In control conditions (before carbachol application), we found that most ROIs did not show any correlated Ca^{2+} activity, as evidenced by a low percentage of correlated ROIs ($|R| < 0.9$) and a mean Pearson correlation coefficient R value of 0.54 ± 0.24 (Fig. 4e-g). As expected for a carbachol application experiment, which forces the simultaneous activation of oligodendroglia (Fig. 4a), we observed a significant overall increase of the positive inter-ROI Ca^{2+} activity correlation level (Fig. 4e-g), with a mean Pearson correlation value of 0.82 ± 0.04 in the presence of carbachol. These results confirmed that the post-prOccam software successfully determined the level of Ca^{2+} activity correlation between ROIs and was able to detect simultaneous increases of that activity as induced by pharmacological agents. In order to adapt to any specifics of biological applications, the Pearson correlation R value threshold might be configured. The percentage of correlated ROIs as well as the mean Pearson correlation coefficient are reported for each image stack in the corresponding output file generated by the post-prOccam.

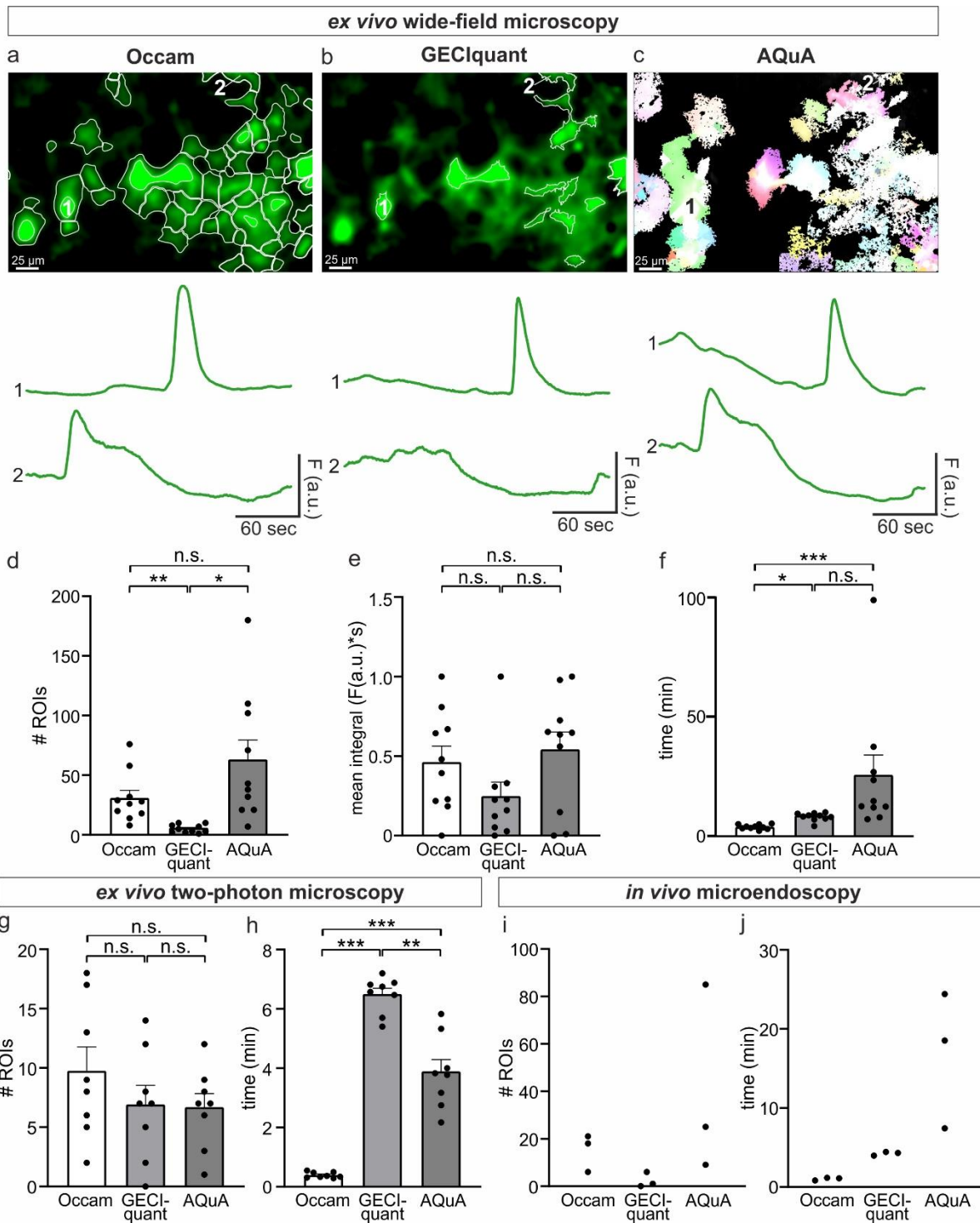
Finally, for informational and debugging purposes, a log file is produced by post-prOccam with a highly detailed account of all the data processing steps and their outcome. The accepted ROIs and the corresponding processed data of a stack are saved by post-prOccam in two separate files for further statistical analysis. Of note is our helper pp-supervisor program that allows the scientist to run post-prOccam automatically over a set of stack data directories, all located in a single master directory. The program either picks the configuration file located in each stack data directory or can be instructed to use the same configuration file located elsewhere. Taken together, the Occam and the post-prOccam software programs provide a configurable and automatable solution for the analysis of oligodendroglial Ca^{2+} signals.

481

482 **Comparison of the capabilities of our package with those of other programs**

483 Occam was compared to two other available programs, GECIquant and AQuA (Venugopal et al.,
484 2019; Wang et al., 2019) using three different imaging datasets wide-field, two-photon, and miniscope.
485 Both GECIquant and AQuA are Fiji/Imagej2 plugins that have recently been employed for the analysis of
486 Ca^{2+} signals in oligodendroglia (Li et al., 2022; Lu et al., 2023). To perform an unbiased comparison, we
487 kept the same parameters of spatial and temporal resolution and minimum pixel size of ROIs, and we
488 optimally tuned the other parameters for each method. Figure 5a-c illustrate the ROIs detected by the
489 three programs in a wide-field oligodendroglia Ca^{2+} imaging stack. Of note, because event detection by
490 AQuA does not use a ROI-based approach, we considered the trajectory of events as ROIs for the
491 comparison (Fig. 5c). We found no significant difference between either the number of ROIs and their
492 localization in the image as detected by AQuA and Occam (Fig. 5a, c, d; % of area occupied by AQuA
493 $(30.8 \pm 1.6\%)$ and Occam $(40.9 \pm 1.2\%)$, Paired t test, $p=0.116$). We noted that AQuA tended to recognize
494 more ROIs than Occam in some stacks and, conversely, GECIquant detected a significantly smaller number
495 of ROIs as compared to both Occam and AQuA (Fig. 5a-d). The normalized mean integral of all detected
496 ROIs was not significantly different between the three programs, which was expected since this value is
497 independent of the number of ROIs (Fig. 5e). However, an interesting observation is that the three tested
498 programs did perform differently in terms of photobleaching correction, with Occam performing a better
499 photobleaching correction than both GECIquant and AQuA, as assessed by manual inspection of the
500 results (Fig. 5a-c, traces). A proper photobleaching correction is desirable when performing analyses on
501 Ca^{2+} imaging datasets obtained in experiments in which drugs are applied because the photobleaching
502 might mask the appearance of the drug effects. Similar results were obtained in *in vivo* microendoscopy
503 datasets where the number of ROIs detected by GECIquant was very low as compared to Occam and AQuA
504 (Fig. 5i). Moreover, manual scrutiny of AQuA results showed that it overestimated the number of events

505 detected in one *in vivo* microendoscopy Ca²⁺ imaging stack where events are detected in regions of the
506 field showing weak regular fluctuations in background illumination, but do not correspond to Ca²⁺
507 transients (Fig. 5i), but it was not possible to find better parameters to optimize the detection. While
508 Occam appears to perform a more faithful ROI detection and photobleaching correction on wide-field
509 imaging stacks from both wide-field and miniscope Ca²⁺ imaging, all three programs detected similar
510 number of ROIs in two-photon imaging stacks (Fig. 5g). Overall, Occam is distinctly more flexible in the
511 analysis of widely differing image stacks originating from different imaging conditions. This observation is
512 consistent with the fact that GECIquant and AQuA were designed and have mainly been used for two-
513 photon Ca²⁺ imaging. From an operational point of view, Occam required significantly less manual input
514 from the user and was more than four times faster (up to 30 times faster) than the other two programs
515 (Fig. 5f, h, j). Occam's speed is an advantage when analyzing a large number of stacks as it makes the
516 analysis more systematic. Compared to AQuA, not only does Occam use less random-access memory
517 (RAM), but it also occupied much less disk space. For comparison, Occam's analysis of three miniscope
518 Ca²⁺ imaging stacks used 1 GB compared to 30 GB for AQuA (0.53 GB for GECIquant). This makes the
519 analysis with Occam easily feasible on any personal computer and more suitable for miniscope data which
520 often relies on large image stacks and data acquired over multiple imaging sessions.



521
522

523 **Figure 5. Comparison of Occam, GECIquant and AQuA for the analysis of wide-field, two-photon and**
 524 **miniscope oligodendroglial Ca²⁺ imaging data.** Representative ROI detection and Ca²⁺ traces obtained by
 525 analysis with Occam (a), GECIquant (b) and AQuA (c). ROI number (d), normalized mean integrals (e) and
 526 time of analysis per stack (f) obtained with Occam, GECIquant and AQuA in wide-field imaging. ROI
 527 number (g) and time of analysis per stack (h) for two-photon imaging and ROI number (i) and time of
 528 analysis (j) for miniscope obtained with Occam, GECIquant and AQuA. No statistical test was applied for

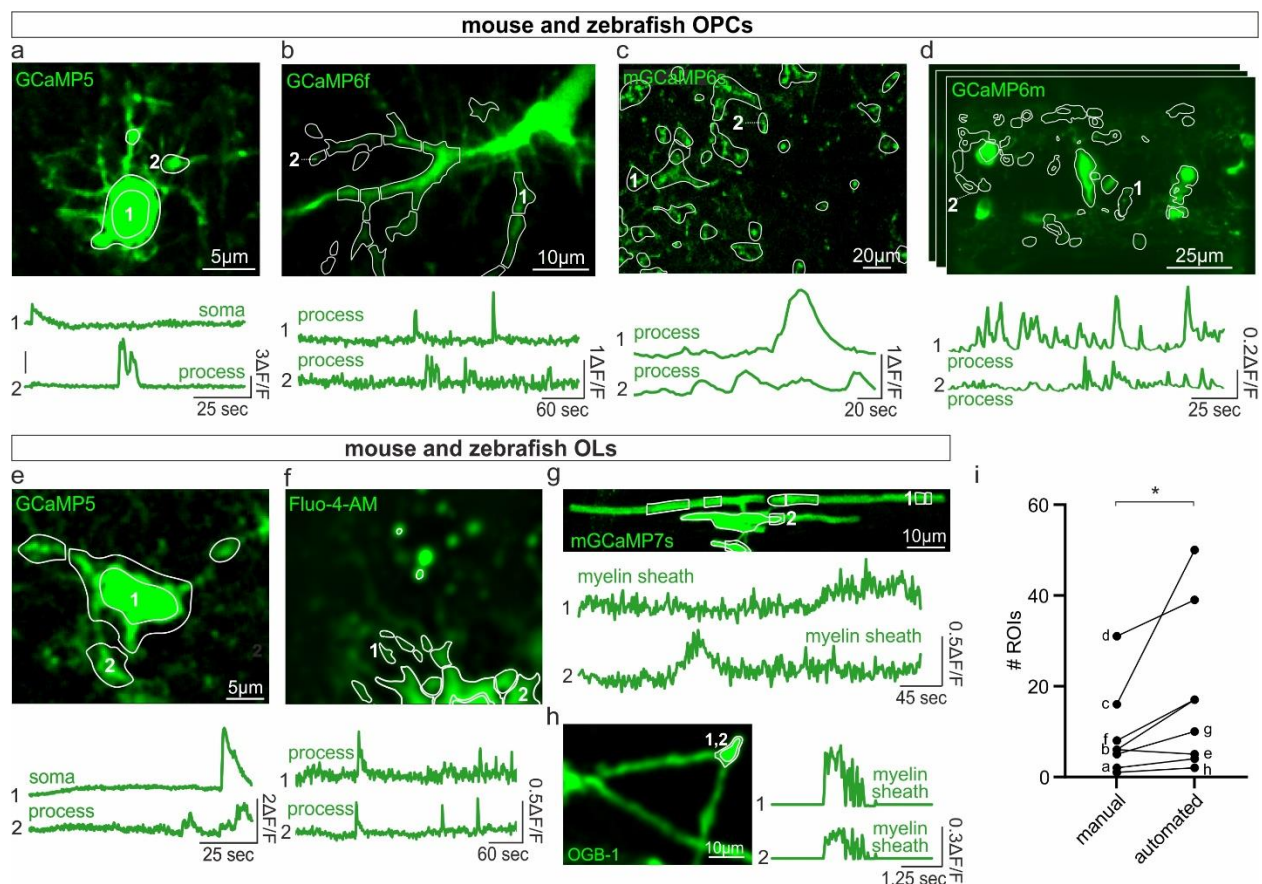
529 miniscope data since the n size was small. n.s.: not significant. * $p < 0.05$, ** $p < 0.01$, *** $p < 0.001$ one-way
530 ANOVA test followed by a Tukey's multiple comparison test or the non-parametric Friedman test followed
531 by a Dunn's multiple comparison test. Dot plots are presented as mean \pm s.e.m.
532

533 **Occam and post-prOccam analyze Ca²⁺ signals from OPCs, OLs and myelin sheaths in diverse species and** 534 **imaging conditions**

535 We sought to validate whether Occam and post-prOccam could successfully analyze Ca²⁺ signals
536 from different cells of the OL lineage, in different species and preparations. Therefore, we used our
537 software to analyze the Ca²⁺ activity of OPCs, OLs and myelin sheaths from our own data as well as data
538 obtained in other laboratories. Our software did analyze independent Ca²⁺ signals both in the soma and
539 fine processes of OPCs from mouse corpus callosum slices following demyelination (Fig. 6a; our own data)
540 and from *in vivo* mouse somatosensory cortex in control (Fig. 6b; Fiore et al., 2022). Notably, when
541 analyzing a wider field of view in the *in vivo* mouse visual cortex (Fig. 6c; Lu et al., 2023) or in the *in vivo*
542 zebrafish spinal cord (Fig. 6d; Bispo & Czopka, unpublished data), our software detected Ca²⁺ activity in
543 fine OPC processes not visibly connected to a soma. Occam and post-prOccam analyzed only active areas
544 of the OPCs, excluding inactive areas of the OPCs that nevertheless exhibited a constant fluorescence. The
545 programs also performed well when analyzing Ca²⁺ activity in image stacks obtained in the soma and
546 processes of OLs recorded in mouse demyelinated lesions in acute slices (Fig. 6e; our own data) and in
547 primary mouse cell cultures (Fig. 6f; Iyer et al., 2023). Finally, it performs equally well in detecting ROIs in
548 myelin sheaths recorded *in vivo* in the zebrafish spinal cord (Fig. 6g; Braaker & Lyons, unpublished data)
549 and the mouse somatosensory cortex (Fig. 6h; Supplementary Video 1 from Bettefeld et al., 2019). To test
550 the performance of our software, we further compared the number of active ROIs that could be
551 distinguished by visual inspection in single cells with that of the active ROIs automatically detected. We
552 found that the automated analysis yields significantly more active ROIs (Fig. 6i).

553 Taken together, these results show that Occam and post-prOccam detect Ca²⁺ events in soma and
554 process of OPCs, OLs and in myelin sheaths from diverse preparations in healthy and pathological

555 conditions. Additionally, Occam and post-prOccam analyzed various Ca^{2+} indicators, including cytosolic
 556 (Fig. 6a, b, e, f, h) and membrane-bound Ca^{2+} indicators (Fig. 6c, d, g).



557
 558
 559 **Figure 6. Occam and post-prOccam analyze Ca^{2+} signals from OPCs, OLs and myelin sheaths in different**
 560 **species and imaging conditions.** Representative images with ROIs (white) and Ca^{2+} traces obtained with
 561 Occam and post-prOccam for (a) a putative OPC from mouse demyelinated corpus callosum in acute slices
 562 recorded in a two-photon microscope (see Materials and Methods), (b) an OPC from the *in vivo* mouse
 563 somatosensory cortex recorded with a two-photon microscope (Supplementary Video 1 from Fiore et al.,
 564 2022), (c) OPC processes from the *in vivo* mouse visual cortex recorded with a two-photon microscope
 565 (Supplementary Video 3 from Lu et al., 2023), (d) OPC somata and processes from the *in vivo* zebrafish
 566 spinal cord recorded with a lightsheet microscope (from Tim Czopka & Patricia Bishop, Unpublished data),
 567 (e) a putative OL from mouse demyelinated corpus callosum in acute slices recorded with a two-photon
 568 microscope (see Materials and Methods), (f) a primary mouse OL in culture recorded with an Opterra II
 569 Multipoint Swept Field Confocal microscope (Supplementary Video 1 from Iyer et al., 2023), (g) an OL
 570 process from the *in vivo* zebrafish spinal cord recorded with a Confocal Zeiss LSM880 Airyscan (from
 571 Philipp Braaker and David Lyons, unpublished data) and (h) an OL process recorded in an acute brain slice
 572 from a mouse with an Olympus BX61WI microscope and a NeuroCCD camera at 40 Hz (Supplementary
 573 Video 1 from Bettefeld et al., 2019). The image stacks were recorded at different acquisition rates and
 574 analysed with Occam using either two-photon (a, b, c, f, g) or miniscope configuration (d). (i) Comparison
 575 of the number of ROIs identified by visual inspection with that of ROIs automatically detected in the
 576 different analyzed stacks. * $p < 0.05$; Wilcoxon rank test. Dot plots are presented as mean \pm s.e.m.

577 **Discussion**

578 While it is suspected that oligodendroglial Ca^{2+} activity plays a key role in myelination and myelin
579 repair, the characteristics of oligodendroglial Ca^{2+} signals remain largely unexplored. This is due to a
580 limited number of *ex vivo* and *in vivo* Ca^{2+} imaging studies as well as a lack of automated imaging data
581 analysis programs adapted to the monitoring of the specific characteristics of oligodendroglial Ca^{2+} signals.
582 To fill this need, we developed a software package comprising two programs, Occam and post-prOccam,
583 that implement an analytical workflow for the automated in-depth analysis of one- and two-photon
584 oligodendroglial Ca^{2+} imaging data. Tested in MS Windows (version 10) and Debian GNU/Linux (versions
585 10 and 11), this cross-platform software was designed to be easily configurable to ensure an unbiased
586 selection of active ROIs and to allow the analysis of large datasets. Licensed under the GNU GPLv3+ Free
587 Software license, both programs can be freely used, modified according to any specific need and question,
588 and redistributed.

589 Because our software package has been developed for our specific needs in Ca^{2+} imaging data
590 analysis of oligodendroglial cells, it performs optimally with this kind of data. It is worthwhile noting that,
591 because the Ca^{2+} signal detection is finely configurable, our software may be suited to new use cases such
592 as the study of other glial cell types. Occam's features for *in vivo* experiments have been adapted so that
593 it could detect not only fast-occurring events, but also the repeated activation of a single region over a
594 long experiment. Occam could successfully and quickly analyze long microendoscopy recordings taken
595 repeatedly over a period of weeks on the same mouse. These results pave the way for future research on
596 oligodendroglia Ca^{2+} signaling in the living mammalian brain during animal behavior studies and in
597 different experimental conditions. Of note, potential motion artifacts may occur in the recordings due to
598 movements of the slice (*ex vivo*) in the recording chamber or the brain (*in vivo*) during behavior. Image
599 distortions caused by motion can be dealt with, prior to Ca^{2+} analysis, by using existing tools such as
600 StackReg and Turboreg ImageJ plugins (Thevenaz et al., 1998).

601 During post-prOccam data processing, false positive ROIs with too small Ca^{2+} fluctuations are
602 rejected, which can be construed as a refinement of the ROI detection process. We found that this
603 automatic Ca^{2+} trace selection performs equally well as a manual Ca^{2+} trace selection. Among other
604 analysis options, the ability to restrict the processing and quantification steps to specific acquisition
605 intervals has proven useful to screen the effect of drugs on oligodendroglial Ca^{2+} signaling. Furthermore,
606 inter-ROI correlation calculations by post-prOccam help make it possible to spotting synchronized Ca^{2+}
607 signals across different ROIs in a given image stack. We validated these analysis modalities by successfully
608 detecting, quantifying and correlating Ca^{2+} activity increases upon carbachol bath application to *ex vivo*
609 mouse brain slices. The implementation of a correlation analysis prompts future research into the
610 synchronization and propagation of Ca^{2+} signals within and between OL lineage cells.

611 Ca^{2+} events of OPCs and OLs are unique in their variability and duration. Unlike neurons, which
612 exhibit well-defined Ca^{2+} signals on a millisecond scale (Chua & Morrison, 2016), both OPCs and OLs show
613 complex Ca^{2+} events characterized by very slow and variable kinetics that make their detection and
614 isolation difficult, particularly because of their frequent convolution (Supplementary Fig. 4). We therefore
615 found that it was easier to quantify them using ROI-based measurable dimensions, such as the number of
616 ROIs, size and mean pixel intensity integral, than using the frequency, amplitude and duration of isolated
617 events. This complexity of oligodendroglia Ca^{2+} events has previously been observed with two-photon
618 microscopy (Balía et al., 2017) and in recordings at single cell resolution (Baraban et al., 2018; Battefeld
619 et al., 2019; Krasnow et al., 2018; Marisca et al., 2020), indicating that complex Ca^{2+} dynamics are a
620 hallmark of OL lineage cells. Thresholding techniques or event template detection methods, commonly
621 used on neuron and astrocyte Ca^{2+} imaging datasets, are not easily applicable to the unique and complex
622 Ca^{2+} events observed in oligodendroglia. For this reason, we evaluate activity levels by measuring the
623 number and size of active ROIs as well as the integral of the traces. Our measurements thus account for
624 the activity throughout the whole ROI trace or during configurable intervals without isolating Ca^{2+} activity

625 events. However, integral values take more into account spatial than temporal features of Ca²⁺ events,
626 and the latter may be important for OL lineage cells under certain conditions (Baraban et al., 2018). In this
627 case, the user could define successive intervals in the post-prOccam configuration file to analyze the
628 evolution of the integral over time for a single stack. In the eventuality that a detailed description of Ca²⁺
629 events would be desirable, extra measurements may be performed either manually or by other post-
630 processing programs on the corrected active ROI traces as output by post-prOccam. Supplementary Figure
631 5 illustrate the analysis of individual Ca²⁺ events for our datasets acquired in the three different conditions,
632 *i.e* wide-field, two-photon and miniscope. Although the complexity of events is largely underestimated in
633 these analyses, it is clear that the duration of Ca²⁺ events lasted from a few seconds to minutes,
634 independent of the imaging condition (see also traces examples in Supplementary Fig. 4 and 5). These
635 slow kinetics are consistent with the long half-width duration of 9 s reported for myelin internodes in the
636 neocortex (Battfeld et al., 2019). It should be noted that the temporal resolution to detect some Ca²⁺
637 events of OL lineage cells may require high acquisition rates (>10 Hz), particularly at the level of myelin
638 sheaths (Battfeld et al., 2019). Although Occam's development was based on stacks acquired at rates
639 between 1.75 Hz and 10 Hz, it properly process image stacks at high frequencies (40Hz; Fig. 6h). In fact,
640 Occam's performance is independent on the acquisition rate since the segmentation to detect active ROIs
641 mainly depends on the quality of the projection images regardless the number of frames. Nevertheless, if
642 Ca²⁺ events are very brief, we recommend using the 'miniscope configuration' as performed for
643 simulations of objects changing location (Supplementary Fig. 2b-c). In addition, the user must define the
644 parameters of the configuration file of post-prOccam according to the acquisition rate and the average
645 kinetics of Ca²⁺ events in order to adjust the post-processing to a fast acquisition condition (see
646 Supplementary files).

647 In the present study, Occam was able to perform ROI detection and bleaching correction not only
648 in two-photon imaging, but also in *ex vivo* and *in vivo* wide-field imaging conditions that have a low signal-

649 to-noise ratio. In addition, Occam performed analyses faster than GECIquant and AQuA, demanded low
650 memory and disk space. We also demonstrated that our software could successfully detect independent
651 fluctuating Ca^{2+} signals in both the soma and the processes of OPCs and OLs, as well as in myelin sheaths,
652 while not taking into account constant fluorescence. Notably, our programs can analyze various Ca^{2+}
653 indicators including GCaMP5, GCaMP6f, GCaMP6s, mGCaMP6s, GCaMP6m, FLUO-4-AM, mGCaMP7s and
654 OGB-1. Together with the software's ability to analyze image stacks obtained in wide-field and two-
655 photon microscopy at different magnifications and from different imaging devices, these results confirm
656 the versatility and reliability of the software. Oligodendroglia from healthy control, pathological and Ca^{2+}
657 activity-stimulated conditions could be analyzed, emphasizing the wide applicability of our analytical
658 workflow. Of note, since image processing is not exactly the same in the different configurations of Occam,
659 we recommend that users test the different configurations to find the one that best handles their data.

660 In conclusion, the presented imaging data analytical software will aid future investigations into
661 the role of OPC and OL Ca^{2+} signaling. As such, it might contribute to the elucidation of Ca^{2+} -related
662 mechanisms implicated in OL lineage cell function and dysfunction which could be relevant to understand
663 the myelination process in healthy and diseased conditions.

664

665

666 **Declarations**

667 **Ethics approval**

668 All experiments followed European Union and institutional guidelines for the care and use of laboratory
669 animals and were approved by both the French ethical committee for animal care of the University Paris
670 Cité (Paris, France) and the Ministry of National Education and Research (Authorization N° 13093-
671 2017081713462292).

672

673 **Consent for publication**

674 All authors have given consent for publication.

675

676 **Availability of data and material**

677 The data generated and analyzed during this study are included in the manuscript and supplementary
678 files. Occam and post-prOccam programs as well as all the software documentation and a full example of
679 ex vivo wide-field imaging data are hosted at <https://gitlab.com/d5674/occam> and published under a Free
680 Software GNU GPLv3+ license.

681

682 **Competing interests**

683 The authors have declared that no competing interests exist.

684

685 **Funding**

686 This work was supported by grants from a subaward agreement from the University of Connecticut with
687 funds provided by Grant No. RG-1612-26501 from National Multiple Sclerosis Society (NMSS), Fondation
688 pour l'aide à la recherche sur la Sclérose en Plaques (ARSEP), Fondation pour la Recherche Médicale (FRM,
689 EQU202103012626), ANR under the frame of the European Joint Programme on Rare Diseases (EJP RD,

690 project no. ANR-19-RAR4-008-03) and ANR CoLD (ANR, ANR-20-CE16-0001-01). D.A.M. received a
691 postdoctoral fellowship from Fondation pour la Recherche Medicale (FRM, project SPF202005011919)
692 and a L'Oréal-UNESCO young talents award 2021 for women in science, B. M.-S. received a PhD fellowship
693 from Université Paris Cité, C.H. received a postdoctoral fellowship from ARSEP. M.C.A. and F.R. are CNRS
694 (Centre National de la Recherche Scientifique) investigators.

695

696 **Authors' contributions**

697 D.A.M. and B. M-S. conducted wide-field Ca^{2+} imaging experiments. C.H. performed two-photon Ca^{2+}
698 imaging experiments and D.A.M. performed *in vivo* microendoscopy Ca^{2+} imaging experiments. D.A.M., B.
699 M-S., C.H. and M.C.A. designed experiments and analysis. P.B., D.A.M., B. M-S wrote the FIJI/ImageJ
700 plugin. M.C.A. and F.R. designed the Python software and F.R. wrote the code. D.A.M. and M.C.A.
701 performed data analyses and D.A.M., F.R. and M.C.A. wrote the manuscript. M.C.A supervised the project.

702

703 **Acknowledgements:**

704 We thank the Neurlmag platform and the animal facility of IPNP and their funding sources (Fédération
705 pour la Recherche Médicale, Fondation Leducq). We would also like to thank Serge Charpak and Yannick
706 Goulam for their help with the two-photon microscope, Callum White for his contribution to initial data
707 analysis in Python and Anastassia Voronova for sharing the protocol for CPZ-induced demyelination. A
708 particular thank to David Lyons and Philipp Braaker, Tim Czopka and Patricia Bispo, Dwight Bergles, Brad
709 Zucchero, Amit Argawal for sharing their Ca^{2+} imaging data and allowing us to test our software
710 capabilities in OPCs and OLs recorded with different Ca^{2+} indicators and in different species and imaging
711 conditions.

712

713 **References**

- 714 Abiraman, K., Pol, S. U., O'Bara, M. A., Chen, G.-D., Khaku, Z. M., Wang, J., Thorn, D., Vedia, B. H.,
715 Ekwegbalu, E. C., Li, J.-X., Salvi, R. J., & Sim, F. J. (2015). Anti-muscarinic adjunct therapy
716 accelerates functional human oligodendrocyte repair. *The Journal of Neuroscience: The Official
717 Journal of the Society for Neuroscience*, 35(8), 3676–3688.
718 <https://doi.org/10.1523/JNEUROSCI.3510-14.2015>
- 719 Agarwal, A., Wu, P.-H., Hughes, E. G., Fukaya, M., Tischfield, M. A., Langseth, A. J., Wirtz, D., & Bergles, D.
720 E. (2017). Transient Opening of the Mitochondrial Permeability Transition Pore Induces
721 Microdomain Calcium Transients in Astrocyte Processes. *Neuron*, 93(3), 587-605.e7.
722 <https://doi.org/10.1016/j.neuron.2016.12.034>
- 723 Arganda-Carreras, I., Kaynig, V., Rueden, C., Eliceiri, K. W., Schindelin, J., Cardona, A., & Sebastian Seung,
724 H. (2017). Trainable Weka Segmentation: A machine learning tool for microscopy pixel
725 classification. *Bioinformatics*, 33(15), 2424–2426. <https://doi.org/10.1093/bioinformatics/btx180>
- 726 Balia, M., Benamer, N., & Angulo, M. C. (2017). A specific GABAergic synapse onto oligodendrocyte
727 precursors does not regulate cortical oligodendrogenesis. *Glia*, 65(11), 1821–1832.
728 <https://doi.org/10.1002/glia.23197>
- 729 Baraban, M., Koudelka, S., & Lyons, D. A. (2018). Ca (2+) activity signatures of myelin sheath formation
730 and growth in vivo. *Nature Neuroscience*, 21(1), 1. PubMed. [https://doi.org/10.1038/s41593-017-](https://doi.org/10.1038/s41593-017-0040-x)
731 [0040-x](https://doi.org/10.1038/s41593-017-0040-x)
- 732 Battefeld, A., Popovic, M. A., de Vries, S. I., & Kole, M. H. P. (2019). High-Frequency Microdomain Ca(2+)
733 Transients and Waves during Early Myelin Internode Remodeling. *Cell Reports*, 26(1), 1. PubMed.
734 <https://doi.org/10.1016/j.celrep.2018.12.039>
- 735 Bjørnstad, D.M., Åbjørnsbråten, K.S., Hennestad, E., Cunen, C., Hermansen, G.H., Bojarskaite, L., Pettersen,
736 K.H., Vervaeke, K., Enger, R. (2021). Begonia-A Two-Photon Imaging Analysis Pipeline for

737 Astrocytic Ca^{2+} Signals. *Frontiers in Cellular Neuroscience*, 15:681066.
738 <https://doi.org/10.3389/fncel.2021.681066>.

739 Cai, D. J., Aharoni, D., Shuman, T., Shobe, J., Biane, J., Song, W., Wei, B., Veshkini, M., La-Vu, M., Lou, J.,
740 Flores, S. E., Kim, I., Sano, Y., Zhou, M., Baumgaertel, K., Lavi, A., Kamata, M., Tuszyński, M.,
741 Mayford, M., ... Silva, A. J. (2016). A shared neural ensemble links distinct contextual memories
742 encoded close in time. *Nature*, 534(7605), 115–118. <https://doi.org/10.1038/nature17955>

743 Cantu, D. A., Wang, B., Gongwer, M. W., He, C. X., Goel, A., Suresh, A., Kourdougli, N., Arroyo, E. D., Zeiger,
744 W., & Portera-Cailliau, C. (2020). EZcalcium: Open-Source Toolbox for Analysis of Calcium Imaging
745 Data. *Frontiers in Neural Circuits*, 14, 25. <https://doi.org/10.3389/fncir.2020.00025>

746 Chua, Y., & Morrison, A. (2016). Effects of Calcium Spikes in the Layer 5 Pyramidal Neuron on Coincidence
747 Detection and Activity Propagation. *Frontiers in Computational Neuroscience*, 10.
748 <https://doi.org/10.3389/fncom.2016.00076>

749 Cohen, R. I., & Almazan, G. (1994). Rat oligodendrocytes express muscarinic receptors coupled to
750 phosphoinositide hydrolysis and adenylyl cyclase. *The European Journal of Neuroscience*, 6(7),
751 1213–1224. <https://doi.org/10.1111/j.1460-9568.1994.tb00620.x>

752 Deshmukh, V. A., Tardif, V., Lyssiotis, C. A., Green, C. C., Kerman, B., Kim, H. J., Padmanabhan, K., Swoboda,
753 J. G., Ahmad, I., Kondo, T., Gage, F. H., Theofilopoulos, A. N., Lawson, B. R., Schultz, P. G., & Lairson,
754 L. L. (2013). A regenerative approach to the treatment of multiple sclerosis. *Nature*, 502(7471),
755 327–332. <https://doi.org/10.1038/nature12647>

756 Fiore, F., Dereddi, R. R., Alhalaseh, K., Coban, I., Harb, A., & Agarwal, A. (2022). *Norepinephrine regulates*
757 *Ca²⁺ signals and fate of oligodendrocyte progenitor cells in the cortex* [Preprint]. BioRx.
758 <https://doi.org/10.1101/2022.08.31.505555>

759 Giovannucci, A., Friedrich, J., Gunn, P., Kalfon, J., Brown, B. L., Koay, S. A., Taxidis, J., Najafi, F., Gauthier,
760 J. L., Zhou, P., Khakh, B. S., Tank, D. W., Chklovskii, D. B., & Pnevmatikakis, E. A. (2019). CalmAn an

761 open source tool for scalable calcium imaging data analysis. *ELife*, 8, e38173.
762 <https://doi.org/10.7554/eLife.38173>

763 Green, A. J., Gelfand, J. M., Cree, B. A., Bevan, C., Boscardin, W. J., Mei, F., Inman, J., Arnow, S., Devereux,
764 M., Abounasr, A., Nobuta, H., Zhu, A., Friessen, M., Gerona, R., von Büdingen, H. C., Henry, R. G.,
765 Hauser, S. L., & Chan, J. R. (2017). Clemastine fumarate as a remyelinating therapy for multiple
766 sclerosis (ReBUILD): A randomised, controlled, double-blind, crossover trial. *Lancet (London,*
767 *England)*, 390(10111), 2481–2489. [https://doi.org/10.1016/S0140-6736\(17\)32346-2](https://doi.org/10.1016/S0140-6736(17)32346-2)

768 Ingiosi, A. M., Hayworth, C. R., Harvey, D. O., Singletary, K. G., Rempe, M. J., Wisor, J. P., & Frank, M. G.
769 (2020). A Role for Astroglial Calcium in Mammalian Sleep and Sleep Regulation. *Current Biology*,
770 30(22), 4373-4383.e7. <https://doi.org/10.1016/j.cub.2020.08.052>

771 Iyer, M., Kantarci, H., Ambiel, N., Novak, S.W., Andrade, L.R., Lam, M., Münch, A.E., Yu, X., Khakh, B.S.,
772 Manor, U., Zuchero, J.B. (2023) Oligodendrocyte calcium signaling sculpts myelin sheath
773 morphology. *BioRxiv*. 2023.04.11.536299. <https://doi.org/10.1101/2023.04.11.536299>

774 Koizumi, S. (2010). Synchronization of Ca²⁺ oscillations: Involvement of ATP release in astrocytes:
775 Astrocytic Ca²⁺ oscillations and neuronal activities. *FEBS Journal*, 277(2), 286–292.
776 <https://doi.org/10.1111/j.1742-4658.2009.07438.x>

777 Krasnow, A. M., Ford, M. C., Valdivia, L. E., Wilson, S. W., & Attwell, D. (2018). Regulation of developing
778 myelin sheath elongation by oligodendrocyte calcium transients in vivo. *Nature Neuroscience*,
779 21(1), 1. PubMed. <https://doi.org/10.1038/s41593-017-0031-y>

780 Li, J., Miramontes, T., Czopka, T., & Monk, K. (2022). *Synapses and Ca²⁺ activity in oligodendrocyte*
781 *precursor cells predict where myelin sheaths form* [Preprint]. *BioRxiv*.
782 <https://doi.org/10.1101/2022.03.18.484955>

783 Lu, T.Y., Hanumaihgari, P., Hsu, E.T., Agarwal, A., Kawaguchi, R., Calabresi, P.A., Bergles, D.E. (2023).
784 Norepinephrine modulates calcium dynamics in cortical oligodendrocyte precursor cells

785 promoting proliferation during arousal in mice. *Nature Neuroscience*.
786 <https://doi.org/10.1038/s41593-023-01426-0>.

787 Marisca, R., Hoche, T., Agirre, E., Hoodless, L. J., Barkey, W., Auer, F., Castelo-Branco, G., & Czopka, T.
788 (2020). Functionally distinct subgroups of oligodendrocyte precursor cells integrate neural activity
789 and execute myelin formation. *Nature Neuroscience*, 23(3), 363–374.
790 <https://doi.org/10.1038/s41593-019-0581-2>

791 Ortiz, F. C., Habermacher, C., Graciarena, M., Houry, P.-Y., Nishiyama, A., Nait Oumesmar, B., & Angulo,
792 M. C. (2019). Neuronal activity in vivo enhances functional myelin repair. *JCI Insight*, 5.
793 <https://doi.org/10.1172/jci.insight.123434>

794 Paez, P. M., & Lyons, D. A. (2020). Calcium Signaling in the Oligodendrocyte Lineage: Regulators and
795 Consequences. *Annual Review of Neuroscience*, 43, 163–186. [https://doi.org/10.1146/annurev-
796 neuro-100719-093305](https://doi.org/10.1146/annurev-neuro-100719-093305)

797 Pitman, K. A., & Young, K. M. (2016). Activity-dependent calcium signalling in oligodendrocyte generation.
798 *The International Journal of Biochemistry & Cell Biology*, 77(Pt A), Pt A. PubMed.
799 <https://doi.org/10.1016/j.biocel.2016.05.018>

800 Sahel, A., Ortiz, F. C., Kerninon, C., Maldonado, P. P., Angulo, M. C., & Nait-Oumesmar, B. (2015). Alteration
801 of synaptic connectivity of oligodendrocyte precursor cells following demyelination. *Frontiers in
802 Cellular Neuroscience*, 9, 77–77. PubMed. <https://doi.org/10.3389/fncel.2015.00077>

803 Schindelin, J., Arganda-Carreras, I., Frise, E., Kaynig, V., Longair, M., Pietzsch, T., Preibisch, S., Rueden, C.,
804 Saalfeld, S., Schmid, B., Tinevez, J.-Y., White, D. J., Hartenstein, V., Eliceiri, K., Tomancak, P., &
805 Cardona, A. (2012). Fiji: An open-source platform for biological-image analysis. *Nature Methods*,
806 9(7), 676–682. <https://doi.org/10.1038/nmeth.2019>

807 Shuman, T., Aharoni, D., Cai, D. J., Lee, C. R., Chavlis, S., Page-Harley, L., Vetere, L. M., Feng, Y., Yang, C. Y.,
808 Mollinedo-Gajate, I., Chen, L., Pennington, Z. T., Taxidis, J., Flores, S. E., Cheng, K., Javaherian, M.,

809 Kaba, C. C., Rao, N., La-Vu, M., ... Golshani, P. (2020). Breakdown of spatial coding and interneuron
810 synchronization in epileptic mice. *Nature Neuroscience*, 23(2), 229–238.
811 <https://doi.org/10.1038/s41593-019-0559-0>

812 Thevenaz, P., Ruttimann, U.E., Unser, M. (1998) A pyramid approach to subpixel registration based on
813 intensity. *IEEE Trans Image Process.* 7(1):27-41. <https://doi.org/10.1109/83.650848>

814 Venugopal, S., Srinivasan, R., & Khakh, B. S. (2019). GECIquant: Semi-automated Detection and
815 Quantification of Astrocyte Intracellular Ca²⁺ Signals Monitored with GCaMP6f. In M. De Pittà &
816 H. Berry (Eds.), *Computational Glioscience* (pp. 455–470). Springer International Publishing.
817 https://doi.org/10.1007/978-3-030-00817-8_17

818 Wang, Y., DelRosso, N. V., Vaidyanathan, T. V., Cahill, M. K., Reitman, M. E., Pittolo, S., Mi, X., Yu, G., &
819 Poskanzer, K. E. (2019). Accurate quantification of astrocyte and neurotransmitter fluorescence
820 dynamics for single-cell and population-level physiology. *Nature Neuroscience*, 22(11), 1936–
821 1944. <https://doi.org/10.1038/s41593-019-0492-2>

822 Welliver, R. R., Polanco, J. J., Seidman, R. A., Sinha, A. K., O'Bara, M. A., Khaku, Z. M., Santiago González,
823 D. A., Nishiyama, A., Wess, J., Feltri, M. L., Paez, P. M., & Sim, F. J. (2018). Muscarinic Receptor M
824 ₃ R Signaling Prevents Efficient Remyelination by Human and Mouse Oligodendrocyte Progenitor
825 Cells. *The Journal of Neuroscience*, 38(31), 31. <https://doi.org/10.1523/JNEUROSCI.1862-17.2018>

826 Xu, Y. K. T., Call, C. L., Sulam, J., & Bergles, D. E. (2021). Automated in vivo Tracking of Cortical
827 Oligodendrocytes. *Frontiers in Cellular Neuroscience*, 15, 667595.
828 <https://doi.org/10.3389/fncel.2021.667595>

829